Defect Engineering toward Atomic Co–N_x–C in Hierarchical Graphene for Rechargeable Flexible Solid Zn-Air Batteries

*Cheng Tang, Bin Wang, Hao-Fan Wang, and Qiang Zhang**

Rechargeable flexible solid Zn-air battery, with a high theoretical energy density of 1086 Wh kg^{-1}, is among the most attractive energy technologies for future flexible and wearable electronics; nevertheless, the practical application is greatly hindered by the sluggish oxygen reduction reaction/oxygen evolution reaction (ORR/OER) kinetics on the air electrode. Precious metal-free functionalized carbon materials are widely demonstrated as the most promising candidates, while it still lacks effective synthetic methodology to controllably synthesize carbocatalysts with targeted active sites. This work demonstrates the direct utilization of the intrinsic structural defects in nanocarbon to generate atomically dispersed Co–N_x–C active sites via defect engineering. As-fabricated Co/N/O tri-doped graphene catalysts with highly active sites and hierarchical porous scaffolds exhibit superior ORR/OER bifunctional activities and impressive applications in rechargeable Zn-air batteries. Specifically, when integrated into a rechargeable and flexible solid Zn-air battery, a high open-circuit voltage of 1.44 V, a stable discharge voltage of 1.19 V, and a high energy efficiency of 63% at 1.0 mA cm^{-2} are achieved even under bending. The defect engineering strategy provides a new concept and effective methodology for the full utilization of nanocarbon materials with various structural features and further development of advanced energy materials.

Modern flexible electronics have emerged rapidly to revolutionize our daily life toward high-tech design, multifunctional experience, and friendly use interface in the last few years, such as roll-up displays, bendable smart phones, implantable biosensors, wearable devices, etc.[1] It is increasingly attractive but still in infancy stage with great challenges ahead to develop effective flexible energy conversion and storage devices, which should meet the particular requirements for flexible devices including high energy and power density, safe operation, nontoxic, shape-conformability, excellent flexibility, and durability.[2] Among various candidates, the Zn-air battery with a theoretical energy density as high as 1086 Wh kg^{-1} has been identified as the most promising and relatively mature energy technology.[3] Attractively, the Zn-air battery is low cost, resource abundant, nontoxic, eco-friendly, and safe to handle, due to the aqueous electrolyte and less-reactive Zn metal.[4] Therefore, intensive research interest has been attracted most recently to explore flexible solid-electrolyte Zn-air batteries, including 1D cable/yarn[5] and 2D sandwich/textile planar types.[6]

Nevertheless, the as-obtained flexible Zn-air batteries still suffer from limited energy efficiency and cycling stability, low output power density, and unsatisfactory discharge voltage plateaus, which are dominantly hindered by the sluggish kinetics and poor durability of oxygen reduction reaction and oxygen evolution reaction (ORR/OER) on the air electrode. Highly active, durable, and earth-abundant bifunctional catalysts for ORR/OER are urgently required to replace precious metal catalysts (such as Pt for ORR and Ir/IrO_2 for OER) and improve the performance of Zn-air batteries.[7] To date, various bifunctional catalysts with high activity and low cost have been developed, such as metal oxides/hydroxides/sulfides/nitrides, nanocarbon materials, and their hybrids.[8] Among them, heteroatom-doped nanocarbon materials are attracting ever-growing interest for bifunctional catalysis and Zn-air batteries, contributed from their high activity, excellent flexibility, low cost, and versatile design.[9] The excellent activity of metal-free carbon materials is dominantly attributed to the altered charge[10] or spin distribution[11] in the sp^2 carbon matrix. Additionally, intrinsic defects on the surface of carbon catalysts have been gradually demonstrated to be critical to the electrocatalytic activities.[9e,12] Furthermore, the introduction of transition metal species, even in a trace amount, is demonstrated to significantly enhance the activity and render carbocatalysts more promising.[13] The coordination between metal and heteroatoms in the carbon matrix, especially the Co/Fe–N_x–C moieties, can effectively modify the local electronic structure and thereby optimize the intermediate adsorption, leading to a superior activity comparable to precious metal catalysts.[14] Specific heteroatom-doping and metal coordination at defective edges are suggested to be the most favorable active sites.[9e] Despite the exciting achievements, it still lacks effective and versatile synthetic methodology to controllably fabricate catalysts with targeted active sites at atomic precision,

---

C. Tang, Dr. B. Wang, H.-F. Wang, Prof. Q. Zhang
Beijing Key Laboratory of Green Chemical Reaction Engineering
and Technology
Department of Chemical Engineering
Tsinghua University
Beijing 100084, P. R. China
E-mail: zhang-qiang@mails.tsinghua.edu.cn

The ORCID identification number(s) for the author(s) of this article can be found under https://doi.org/10.1002/adma.201703185.

DOI: 10.1002/adma.201703185

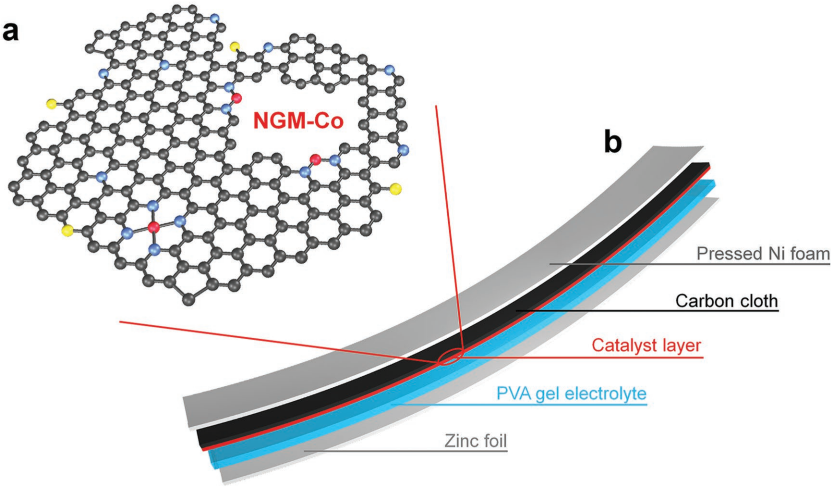

Figure 1. Schematic illustration of the flexible solid Zn-air battery. a) A schematic illustration of the hierarchical Co/N/O tri-doped graphene catalyst (NGM-Co). The grey atom represents for carbon, blue atom represents for nitrogen, yellow atom represents for oxygen, and red atom represents for cobalt. b) A flexible solid Zn-air battery using NGM-Co as the air-cathode catalyst.

such as heteroatom dopants, topological defects, and metal–nitrogen–carbon moieties.

In this contribution, we directly utilize the intrinsic structural defects in nanocarbon to generate atomically dispersed Co–N_x–C active sites via defect engineering. The as-obtained Co/N/O tri-doped graphene mesh (denoted as NGM-Co hereinafter) exhibits a hierarchical porous structure with high density of active sites derived from Co–N_x–C moieties, nitrogen-doping, oxygen functional groups, and topological defects, rendering remarkable bifunctional electrocatalytic activities for both ORR and OER in alkaline. Impressively, when integrated into a rechargeable flexible solid Zn-air battery, a high open-circuit voltage (1.44 V), a small charge/discharge voltage gap (0.7 V at 1.0 mA cm^{-2}), and high energy efficiency (63% at 1.0 mA cm^{-2}) are achieved. The as-assembled flexible solid Zn-air battery also displays excellent cycling durability, with a stable discharge voltage as high as 1.19 V under bending, suggesting a promising application in wearable electronics (**Figure 1**). This work provides fresh insights into the utilization of defects in nanocarbon materials and promotes their applications in the field of materials science and energy conversion.

The NGM-Co was prepared via the direct carbonization of a powdery mixture of gelatinized amylopectin, melamine, cobalt nitrate, and in situ generated $Mg(OH)_2$ nanoflakes (see details in the Supporting Information). A metal-free counterpart was also prepared under otherwise identical conditions without cobalt nitrate (denoted as NGM). The morphology of as-obtained NGM-Co was characterized by scanning electron microscopy (SEM) and transmission electron microscopy (TEM), as shown in **Figure 2**a–d. The graphene flakes are dominantly few-layered with a lateral size of ≈200 nm and abundance of in-plane nanoholes (Figure 2c). They are self-assembled into a hierarchical framework with interconnected large pores, precisely replicating the scaffold of MgO templates (Figure 2a; Figure S1, Supporting Information). The NGM sample fabricated without cobalt nitrate addition possesses the similar structure, suggesting the predominant role of MgO templates on graphitization and morphology replication (Figures S2 and S3, Supporting Information).[12b,15] The structural porosity was further characterized by nitrogen sorption experiments. As revealed in Figure S4 (Supporting Information), a high specific surface area (SSA) of 541.5 m^2 g^{-1} is obtained for NGM-Co, nearly twice that of NGM (271.6 m^2 g^{-1}). Besides, the total pore volume of NGM-Co is calculated to be 1.36 cm^3 g^{-1}, which is ≈30% higher than that of NGM (1.03 cm^3 g^{-1}). More specifically, the micropores and mesopores below 5.0 nm are obviously increased for NGM-Co with respect to the contributions for pore volume and SSA (Figure S5, Supporting Information). Besides, a relatively higher I_D/I_G ratio is obtained from the Raman spectrum for NGM-Co (Figure S6, Supporting Information), indicating more defective sites due to the increased micropores and mesopores. The distinct porosity and structural features can be rationalized by the catalytic and etching effect of cobalt/cobalt oxide nanoparticles during high-temperature carbonization (Figure S7, Supporting Information). Therefore, with the joint roles of MgO templates and cobalt-based nanoparticles, a hierarchical porous graphene material can be facilely obtained with abundant micro/mesosized nanopores in plane and macrosized strutted spaces between sheets, which is beneficial for the mass transfer during triple-phase reactions. In addition, it was theoretically revealed that the metal–N_4 clusters were more energetically feasible to form at graphitic edges.[16] Hence, it is believed that the Co species tend to coordinate with the nitrogen dopants at defective edges or pores of graphene, which are abundant in NGM, leading to a facilely achieved atomic dispersion and superior catalytic performances.

Notably, no obvious nanoparticle in TEM images (Figure 2b,c) or characteristic peaks in X-ray diffraction (XRD) spectroscopy (inset of Figure 2c) can be found corresponding to any cobalt species in NGM-Co, suggesting the thorough dissolution of metallic Co or cobalt oxides after harsh acid treatment (Figure S7, Supporting Information). However, the energy dispersive spectroscopy (EDS) mapping of NGM-Co indicates a weak-signal but uniform distribution of Co, completely superimposed with N and C (Figure S8, Supporting Information). Additionally, the dark field high-resolution TEM image presents a number of highly dispersed bright spots, most likely ascribed to the highly dispersed Co atoms survived (Figure 2d; Figure S9, Supporting Information). To determine the trace amount of cobalt accurately, inductively coupled plasma optical emission spectrometer was conducted, and a low bulk Co content of ≈1.23 wt% was detected. These results strongly suggest a high dispersion of Co atoms in the porous NGM layers with configurations such as Co–N_x–C.

Furthermore, X-ray photoelectron spectroscopy (XPS) was performed to analyze the chemical features in detail. As shown in Figure S10 (Supporting Information), the XPS survey spectra reveal high amounts of nitrogen and oxygen in both NGM-Co

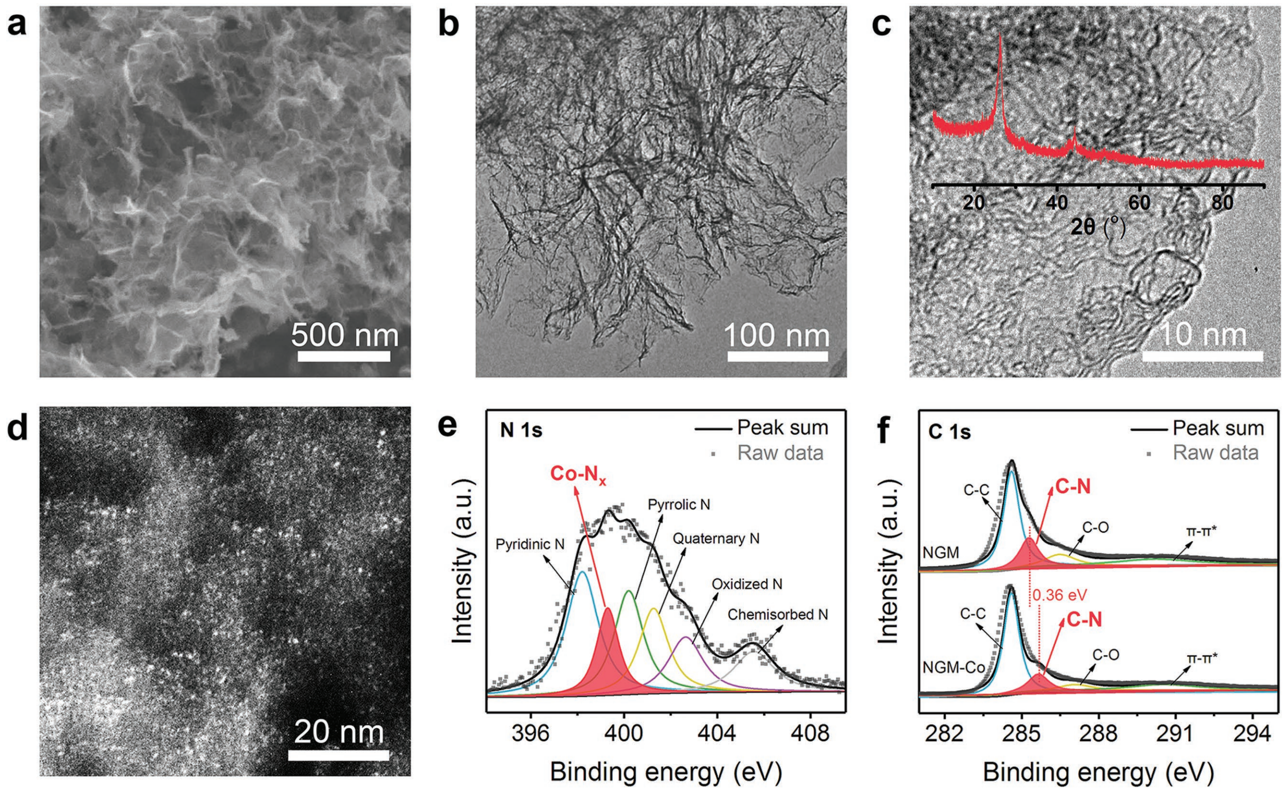

Figure 2. Morphology and composition characterization of NGM-Co catalysts. a) SEM image and b,c) TEM images showing the hierarchical porous framework of NGM-Co. No metal-based nanoparticle can be found. The inset of (c) represents the XRD pattern of NGM-Co without any characteristic peak of cobalt species. d) Dark-field high-resolution TEM image showing highly dispersed Co atoms in graphene layers. XPS spectra of e) N 1s and f) C 1s for NGM-Co, indicating the formation of Co–N$_x$–C configurations.

and NGM samples (N: 2.31 at% for NGM-Co and 4.42 at% for NGM; O: 3.22 at% for NGM-Co and 2.04 at% for NGM), while no significant Co 2p peak can be detected due to its ultralow content (≈0.18 at%), nearly under the detection limit of XPS. It has been widely demonstrated that N, O, or N/O dual-doping plays a crucial role in catalyzing both ORR and OER by altering the electronic distribution of adjacent carbon atoms and facilitating the intermediate adsorption.[9a,d,17] It is notable that a new peak around 399.3 eV has to be included when decomposing the N 1s spectrum for NGM-Co in contrast to NGM (Figure 2e; Figure S11 and Table S1, Supporting Information). It is claimed as the pyridinic N bound to Co (Co–N$_x$–C), with ≈1 eV upshift from pristine pyridinic N (≈398.4 eV).[18] Moreover, the C–N shoulder in the C core spectrum of NGM-Co noticeably shifts to higher binding energy (Figure 2f), which can be rationalized by the strong electron-withdrawing effect of Co coordinated with the nitrogen in Co–N$_x$–C moieties. The decreased electron density of adjacent C atoms is expected to facilitate the adsorption of ORR/OER intermediates and promote the electron transfer for an enhanced kinetics.

The above characterizations reveal the facile and successful synthesis of a graphene catalyst via defect engineering, exhibiting a hierarchical porosity and C/N/O tri-doped features. The Co–N$_x$–C moieties are controllably generated at atomic precision owing to the abundant defective edges for the anchor of Co species and lower formation energy. Along with abundant nitrogen-doping, oxygen functional groups, and topological defects, the NGM-Co catalysts are suggested to be promising for bifunctional ORR/OER electrocatalysis and flexible Zn-air batteries.

The electrocatalytic activity was first investigated by cyclic voltammetry (CV) and linear sweep voltammetry (LSV) measurements on a rotating disk electrode (RDE) in 0.10 M KOH with a mass loading of ≈0.25 mg cm^{-2}. As shown in **Figure 3**a, distinct cathodic peaks are observed for NGM-Co and NGM in O$_2$-saturated electrolyte. The ORR peak current density for NGM-Co is obviously larger and the peak potential is ≈60 mV positively shifted compared with NGM. LSV curves further reveal a much higher limiting current density of 4.75 mA cm^{-2} for NGM-Co than NGM (Figure 3b). Besides, the half-wave potential for NGM-Co is ≈50 mV more positive than NGM, indicating a much better ORR activity with the presence of Co species. Moreover, the Tafel slopes determined from Figure 3c are 58, 119, and 59 mV dec^{-1} for NGM-Co, NGM, and Pt/C, respectively, suggesting the NGM-Co as an excellent ORR catalyst with fast kinetics comparable to Pt/C. Compared with metal-free NGM, the NGM-Co catalyst exhibits similar morphology and types of active sites, merely except for the trace amount of Co–N$_x$–C species. Notably, the nitrogen content for NGM-Co is nearly half that of NGM, which is widely recognized as the main active origin and positively correlated with the catalytic activity for nanocarbon catalysts. However, the ORR performance of NGM-Co is significantly superior to NGM with a higher limiting current density and lower overpotential,

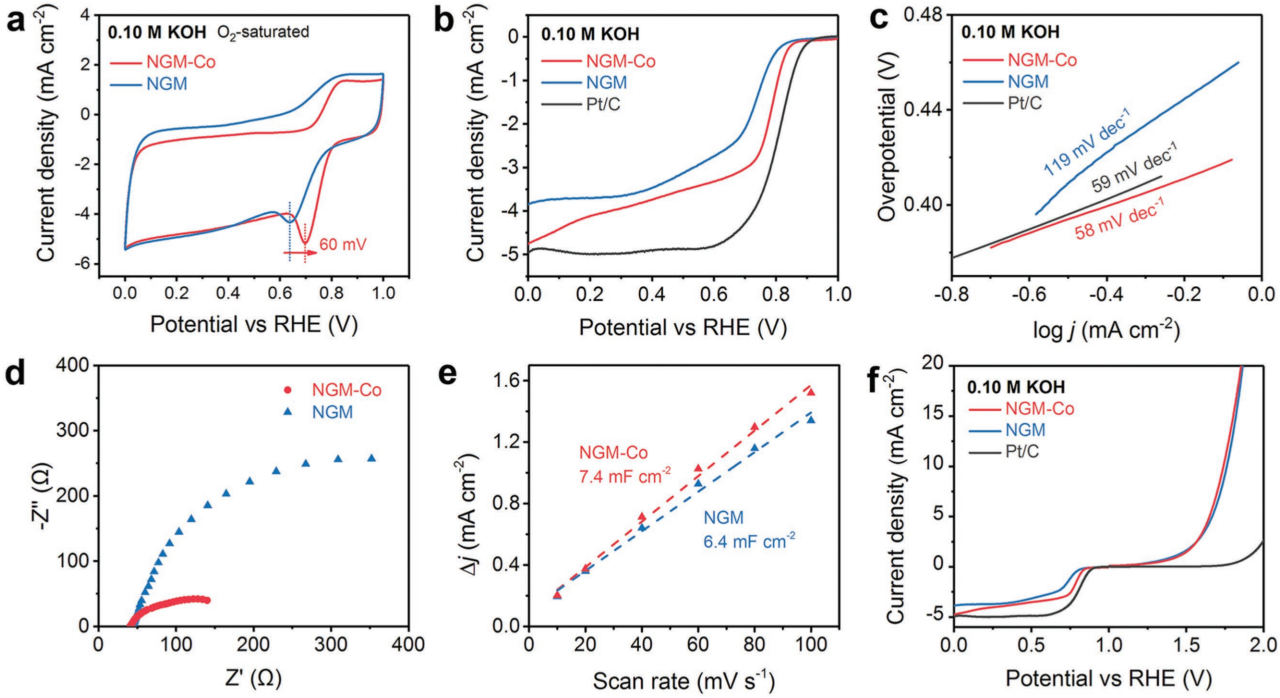

Figure 3. ORR performance and bifunctional activities of NGM-Co catalysts. a) CV curves of NGM-Co and NGM in O_2-saturated 0.10 M KOH with a scan rate of 100.0 mV s^{-1}. b) IR-corrected LSV curves for ORR in O_2-saturated 0.10 M KOH at 1600 rpm (10.0 mV s^{-1}), and c) corresponding Tafel plots. d) Nyquist plots of the impedance for NGM-Co and NGM at a potential of 0.79 V versus RHE. e) Charging current density differences plotted versus scan rate for NGM and NGM-Co. f) LSV curves of different catalysts (10.0 mV s^{-1}), showing the bifunctional ORR/OER catalytic activity. The catalyst loading was ≈0.25 mg cm^{-2} for all tests.

highlighting the critical role of Co–N_x–C species on ORR catalytic activity. The distinct Tafel slope values for NGM-Co and NGM in similar potential ranges further reveal that the reaction mechanism and rate limiting step are changed due to the incorporation of Co–N_x–C active sites.[19]

To elucidate the superior ORR activity of NGM-Co, electrochemical impedance spectroscopy was performed at 0.79 V versus reversible hydrogen electrode (RHE). As shown in Figure 3d, the substantially smaller semicircle in the medium-frequency region clearly reveals a decreased charge transfer resistance for NGM-Co compared with NGM. In addition, the electrochemical active surface area (ECSA) was determined via the scan-rate dependent CV measurements within a potential window of 1.00–1.05 V versus RHE. As revealed in Figure 3e, NGM-Co exhibits a larger ECSA represented by the double-layer capacitance, about 16% higher than NGM. It is contributed from the much higher SSA, enriched micro/mesopores, and improved hydrophilicity for NGM-Co (Figure S12, Supporting Information).

The OER catalytic activity of NGM-Co was also measured in 0.10 M KOH at 1600 rpm. As shown in Figure S13 (Supporting Information), the NGM-Co displays a lower onset potential and much higher current density than Pt/C. Figure 3f clearly represents the good ORR/OER bifunctional activities for NGM-Co, with a low potential difference around 0.95 V between the OER potential for 10.0 mA cm^{-2} and ORR potential at half-wave. Unexpectedly, the OER LSV curves of NGM-Co and NGM are nearly overlapped. There is only 20 mV difference on the overpotential required for a current density of 10.0 mA cm^{-2}. In contrast to the distinct ORR activities, the similar OER performance for NGM-Co and NGM suggests that the optimal active sites for ORR and OER are different. The Co–N_x–C species are demonstrated to be remarkably favorable for ORR, while their effect on OER activity is substantially limited. Therefore, the OER activity is dominantly determined by the nitrogen and oxygen doping,[17a] leading to a similar OER performance between NGM-Co and NGM (Figure S13, Supporting Information).

To evaluate the utility of bifunctional NGM-Co catalysts for flexible solid-state Zn-air batteries, a rechargeable liquid Zn-air battery was first assembled. A Zn foil was used as the anode, and the catalyst-loaded carbon cloth as air-cathode, with a catalyst loading of ≈0.50 mg cm^{-2}. 0.20 M $ZnCl_2$ was added into the 6.0 M KOH aqueous electrolyte to ensure the reversible anode reactions and rechargeable operation.[3b] The commercial state-of-the-art Pt/C for ORR and Ir/C for OER were mixed together as the control catalyst for Zn-air batteries (denoted as Pt/C + Ir/C). As shown in **Figure 4**a, a much higher discharge current and a notably shrunken charge–discharge voltage gap are obtained for the Zn-air battery catalyzed by NGM-Co in comparison with Pt/C + Ir/C, suggesting the superior activity and rechargeability. The maximum power density of the former is determined to be as high as 152 mW cm^{-2}, triple that of Pt/C + Ir/C and among the best performances ever reported (Table S2, Supporting Information).[9b,c,f,20] As an impressive exemplification for practical applications, one Zn-air battery as-assembled based on NGM-Co can power a toy car to drive quickly for some distance (Figure 4b; Movie S1, Supporting Information). When

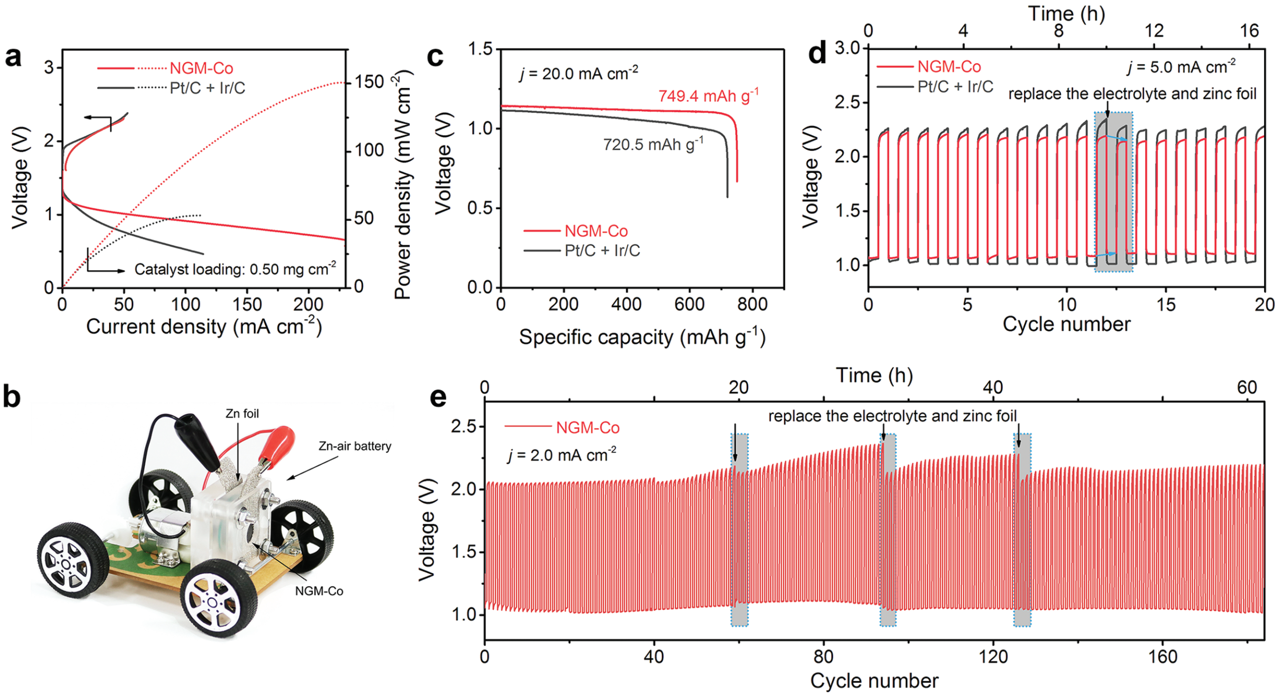

Figure 4. Application of NGM-Co in rechargeable liquid Zn-air batteries. a) Charge and discharge polarization curves. b) Photograph of a toy car powered by one Zn-air battery based on NGM-Co catalyst. c) Discharge curves of Zn-air batteries assembled from the NGM-Co and Pt/C + Ir/C catalysts at 20.0 mA cm^{-2} discharging rate. d) Galvanostatic discharge–charge cycling curves at 5.0 mA cm^{-2} of the rechargeable Zn-air batteries. e) Long time cycling test at 2.0 mA cm^{-2}. The electrolyte and zinc foil were replaced for a subsequent cycling as the arrows noted in (d) and (e).

galvanostatically discharged at 20.0 mA cm^{-2}, the Zn-air battery catalyzed by NGM-Co delivers a stable discharge voltage around 1.12 V without any obvious degradation (Figure 4c). The specific capacity at 20.0 mA cm^{-2} is calculated to be as high as ≈750 mAh g^{-1} normalized to the mass of consumed Zn (≈91.4% utilization of the theoretical capacity 820 mAh g^{-1}), corresponding to a high energy density of ≈840 Wh kg^{-1} based on Zn (≈77.3% of the theoretical energy density 1086 Wh kg^{-1}). These remarkable metrics are the best results ever reported based on precious-metal-free catalysts (Table S2, Supporting Information), and even superior than the precious metal counterpart (Figure 4c), demonstrating the outstanding ORR/OER activities of NGM-Co under working conditions.[9c,f,20b,c,21]

Both rechargeability and cyclic durability are critical for the practical applications of Zn-air batteries. When cycled at a constant current density of 5.0 mA cm^{-2}, the Zn-air battery based on NGM-Co catalysts delivers an initial discharge potential of 1.07 V and a charge potential of 2.19 V (Figure 4d). After 12 cycles (about 10 h), the performance is unexpectedly improved, with a small decrease in the charge/discharge voltage gap by 30 mV. Importantly, the voltage gap can be further decreased by 30% and a high round-trip energy efficiency of 53% can be obtained, if the electrolyte and zinc foil are replaced with fresh ones, revealing the remarkable cycling stability and rechargeability of NGM-Co catalyst itself. By contrast, the Pt/C + Ir/C air-cathode suffers from obvious activity decay during the cycling, probably due to the oxidation and loss of precious metals under the positive charge potential. Furthermore, a long cycling test at a current density of 2.0 mA cm^{-2} was performed using the NGM-Co air-cathode. As shown in Figure 4e, the discharge voltage is stable for more than 60 h, while the charge voltage can be recovered with the electrolyte and Zn refreshed. This strongly indicates a high bifunctional activity and excellent stability of NGM-Co catalysts, which is prerequisite for flexible Zn-air batteries.

On the basis of the promising catalytic activity and liquid battery performance present above, a rechargeable flexible Zn-air battery was fabricated using the NGM-Co coated carbon cloth as air-cathode (catalyst loading: 1.50 mg cm^{-2}), flexible zinc foil as anode, alkaline gel electrolyte, and pressed nickel foam as current collector (Figure 1b). The alkaline poly(vinyl alcohol) (PVA) gel electrolyte is fabricated with KOH, $ZnCl_2$, and PVA in deionized water (see details in the Supporting Information), which is flexible, bendable, and stretchable (Figure S14, Supporting Information), delivering considerable ionic conductivity and mechanical flexibility for flexible Zn-air batteries. The open-circuit voltage is measured to be as high as 1.439 V (**Figure 5**a). Figure 5b shows the charge and discharge polarization curves of the rechargeable flexible Zn-air battery, with a small voltage gap comparable to the liquid battery, suggesting the excellent performance in solid-state batteries as well. As shown in Figure 5c, flat charge/discharge voltage plateaus are achieved at a constant current density of 1.0 mA cm^{-2}, showing prominent activity and utility for flexible solid Zn-air batteries compared with previous reports.[9c] Moreover, the flexible solid Zn-air battery can be cycling charged/discharged at stable potentials for a long time, even when bended to different angles (Figure 5c). It is notable that an impressively low voltage gap of 0.7 V and a high energy efficiency of 63% can be achieved (discharge potential of 1.19 V and charge potential of 1.89 V) for the prepared

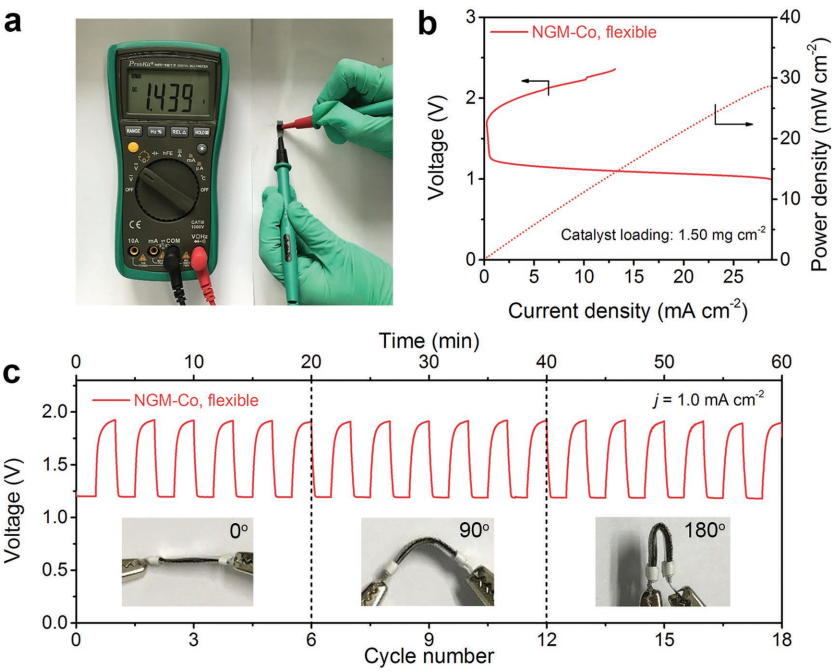

Figure 5. Application of NGM-Co in rechargeable flexible solid Zn-air batteries. a) Photograph of the solid Zn-air battery, showing an open-circuit voltage of 1.439 V. b) Charge and discharge polarization curves. c) Galvanostatic discharge–charge cycling curves at 1.0 mA cm^{-2} under bending.

flexible Zn-air battery. These results reveal that the as-obtained NGM-Co catalyst has attractive potential in the rechargeable and flexible solid Zn-air batteries and wearable devices, bridging the fundamental materials science and practical device integration toward more sustainable, flexible, and smart energy. Notably, in addition to the optimization of cathode catalysts, intense efforts are also urgently required to develop stable Zn anodes, flexible and highly ionic conductive electrolytes, and device components for the practical applications.

The impressive Zn-air battery performances based on NGM-Co are contributed from the unique structural and chemistry features of such precious-metal-free catalyst. The effective MgO-templated carbonization process renders a hierarchical porous graphene scaffold with abundant micro/mesosized nanopores in plane and macrosized strutted spaces between sheets. This structural hierarchy, together with an improved surface hydrophility, is favorable for the mass transfer during catalysis process. Moreover, the abundant defective edges in graphene facilitate the coordination of cobalt atoms with pyridinic N, leading to highly dispersed Co–N$_x$–C species. Consequently, the charge distribution on the sp^2-conjugated carbon matrix is effectively modified by Co–N$_x$–C, N-doping, and oxygen functional groups, toward optimal chemisorption of intermediates and facilitated electron transfer, leading to expected catalytic activities and promising applications in Zn-air battery. Further work is undergoing to optimize the metal–nitrogen–graphene catalysts at atomic precision via as-proposed defect engineering strategy and improve the resultant activity and durability. The as-obtained electrocatalyst is also important for other emerging next-generation batteries (e.g., Li-O$_2$ batteries,[4] Li-N$_2$ batteries,[22] and so on).

In summary, a Co/N/O tri-doped graphene catalyst was facilely fabricated with atomically dispersed Co–N$_x$–C active sites via defect engineering strategy. The as-fabricated catalyst exhibits good ORR/OER bifunctional activities and impressive performances in rechargeable Zn-air batteries. The ORR catalytic activities for NGM-Co are comparable to Pt/C, with a high limiting current density (4.75 mA cm^{-2}) and low Tafel slope (58 mV dec^{-1}). Rechargeable liquid Zn-air batteries are assembled using NGM-Co as cathode catalysts, delivering a maximum power density as high as 152 mW cm^{-2} and a stable discharge voltage around 1.12 V at 20.0 mA cm^{-2}. Furthermore, the NGM-Co is integrated into a rechargeable flexible solid Zn-air battery showing impressive performances. A high open-circuit voltage of 1.44 V, a small charge/discharge voltage gap of 0.7 V, a high energy efficiency of 63% at 1.0 mA cm^{-2}, and a stable discharge voltage of 1.19 V even under bending can be achieved. This work provides novel concept of defect engineering to prepare atomically dispersed Co–N$_x$–C active sites in nanocarbon catalysts, which is instructive for the utilization of structural defects in nanocarbon and other materials, and further development of advanced materials in various applications. The demonstration in rechargeable liquid and flexible solid Zn-air batteries also paves a new way for the development of high-efficient, cost-effective, and environmental-friendly flexible energy conversion and storage devices.

Supporting Information

Supporting Information is available from the Wiley Online Library or from the author.

Acknowledgements

C.T. and B.W. contributed equally to this work. This work was financially supported by National Key Research and Development Program (Grant Nos. 2016YFA0202500, 2016YFA0200102, and 2015CB932500) and Natural Scientific Foundation of China (Grant No. 21422604). The authors thank the helpful discussion from Bo-Quan Li, Xiaoyang Cui, Zi-Jing Xia, Shu-Yuan Zhang, Ling Zhong, and Chen-Yu Chen.

Conflict of Interest

The authors declare no conflict of interest.

Keywords

bifunctional electrocatalysts, defect engineering, oxygen reduction reaction, zinc-air batteries

Received: June 7, 2017
Revised: June 25, 2017

[1] a) W. Liu, M. S. Song, B. Kong, Y. Cui, *Adv. Mater.* **2017**, *29*, 1603436; b) L. Wen, F. Li, H. M. Cheng, *Adv. Mater.* **2016**, *28*, 4306.

[2] a) X. F. Wang, X. H. Lu, B. Liu, D. Chen, Y. X. Tong, G. Z. Shen, *Adv. Mater.* **2014**, *26*, 4763; b) L. Li, Z. Wu, S. Yuan, X. B. Zhang, *Energy Environ. Sci.* **2014**, *7*, 2101; c) S. L. Zhai, H. E. Karahan, L. Wei, Q. Qian, A. T. Harris, A. I. Minett, S. Ramakrishna, A. Keong Ng, Y. Chen, *Energy Storage Mater.* **2016**, *3*, 123; d) A. Sumboja, X. M. Ge, Y. Zong, Z. L. Liu, *Funct. Mater. Lett.* **2016**, *9*, 1630001; e) H.-F. Wang, C. Tang, B. Wang, B.-Q. Li, Q. Zhang, *Adv. Mater.* **2017**, *29*, 1702327.

[3] a) Y. G. Li, H. J. Dai, *Chem. Soc. Rev.* **2014**, *43*, 5257; b) C. Z. Zhang, N. Mahmood, H. Yin, F. Liu, Y. L. Hou, *Adv. Mater.* **2013**, *25*, 4932.

[4] J.-S. Lee, S. T. Kim, R. Cao, N.-S. Choi, M. Liu, K. T. Lee, J. Cho, *Adv. Energy Mater.* **2011**, *1*, 34.

[5] a) J. Park, M. Park, G. Nam, J.-S. Lee, J. Cho, *Adv. Mater.* **2015**, *27*, 1396; b) Y. Xu, Y. Zhang, Z. Guo, J. Ren, Y. Wang, H. Peng, *Angew. Chem., Int. Ed.* **2015**, *54*, 15390; c) F. L. Meng, H. X. Zhong, D. Bao, J. M. Yan, X. B. Zhang, *J. Am. Chem. Soc.* **2016**, *138*, 10226.

[6] a) J. Zhang, J. Fu, X. Song, G. Jiang, H. Zarrin, P. Xu, K. Li, A. Yu, Z. Chen, *Adv. Energy Mater.* **2016**, *6*, 1600476; b) J. Fu, F. M. Hassan, J. Li, D. U. Lee, A. R. Ghannoum, G. Lui, M. A. Hoque, Z. Chen, *Adv. Mater.* **2016**, *28*, 6421; c) J. Fu, D. U. Lee, F. M. Hassan, L. Yang, Z. Bai, M. G. Park, Z. Chen, *Adv. Mater.* **2015**, *27*, 5617; d) M. Yu, Z. Wang, C. Hou, Z. Wang, C. Liang, C. Zhao, Y. Tong, X. Lu, S. Yang, *Adv. Mater.* **2017**, *29*, 1602868; e) J. Fu, J. Zhang, X. Song, H. Zarrin, X. Tian, J. Qiao, L. Rasen, K. Li, Z. Chen, *Energy Environ. Sci.* **2016**, *9*, 663.

[7] J. Fu, Z. P. Cano, M. G. Park, A. P. Yu, M. Fowler, Z. W. Chen, *Adv. Mater.* **2017**, *29*, 1604685.

[8] a) Z.-L. Wang, D. Xu, J.-J. Xu, X.-B. Zhang, *Chem. Soc. Rev.* **2014**, *43*, 7746; b) F. Cheng, J. Chen, *Chem. Soc. Rev.* **2012**, *41*, 2172; c) X. Zhang, X. Cheng, Q. Zhang, *J. Energy Chem.* **2016**, *25*, 967; d) D. U. Lee, P. Xu, Z. P. Cano, A. G. Kashkooli, M. G. Park, Z. Chen, *J. Mater. Chem. A* **2016**, *4*, 7107; e) B.-Q. Li, S.-Y. Zhang, C. Tang, X. Cui, Q. Zhang, *Small* **2017**, *13*, 1700610.

[9] a) K. P. Gong, F. Du, Z. H. Xia, M. Durstock, L. M. Dai, *Science* **2009**, *323*, 760; b) H. B. Yang, J. Miao, S.-F. Hung, J. Chen, H. B. Tao, X. Wang, L. Zhang, R. Chen, J. Gao, H. M. Chen, L. Dai, B. Liu, *Sci. Adv.* **2016**, *2*, e1501122; c) Q. Liu, Y. Wang, L. Dai, J. Yao, *Adv. Mater.* **2016**, *28*, 3000; d) Y. Zhao, R. Nakamura, K. Kamiya, S. Nakanishi, K. Hashimoto, *Nat. Commun.* **2013**, *4*, 2390; e) C. Tang, Q. Zhang, *Adv. Mater.* **2017**, *29*, 1604103; f) J. Zhang, Z. Zhao, Z. Xia, L. Dai, *Nat. Nanotechnol.* **2015**, *10*, 444.

[10] M. T. Li, L. P. Zhang, Q. Xu, J. B. Niu, Z. H. Xia, *J. Catal.* **2014**, *314*, 66.

[11] a) I.-Y. Jeon, S. Zhang, L. Zhang, H.-J. Choi, J.-M. Seo, Z. Xia, L. Dai, J.-B. Baek, *Adv. Mater.* **2013**, *25*, 6138; b) L. Zhang, Z. Xia, *J. Phys. Chem. C* **2011**, *115*, 11170.

[12] a) Y. Jiang, L. Yang, T. Sun, J. Zhao, Z. Lyu, O. Zhuo, X. Wang, Q. Wu, J. Ma, Z. Hu, *ACS Catal.* **2015**, *5*, 6707; b) C. Tang, H.-F. Wang, X. Chen, B.-Q. Li, T.-Z. Hou, B. Zhang, Q. Zhang, M.-M. Titirici, F. Wei, *Adv. Mater.* **2016**, *28*, 6845; c) L. Zhang, Q. Xu, J. Niu, Z. Xia, *Phys. Chem. Chem. Phys.* **2015**, *17*, 16733; d) D. Yan, Y. Li, J. Huo, R. Chen, L. Dai, S. Wang, *Adv. Mater.* **2017**, *29*, 1606459; e) R. Liu, Y. Wang, D. Liu, Y. Zou, S. Wang, *Adv. Mater.* **2017**, *29*, 1701546.

[13] a) G. A. Ferrero, K. Preuss, A. Marinovic, A. B. Jorge, N. Mansor, D. J. L. Brett, A. B. Fuertes, M. Sevilla, M.-M. Titirici, *ACS Nano* **2016**, *10*, 5922; b) Y. Zhao, K. Kamiya, K. Hashimoto, S. Nakanishi, *J. Phys. Chem. C* **2015**, *119*, 2583.

[14] a) P. Chen, T. Zhou, L. Xing, K. Xu, Y. Tong, H. Xie, L. Zhang, W. Yan, W. Chu, C. Wu, Y. Xie, *Angew. Chem., Int. Ed.* **2017**, *56*, 610; b) C. Tang, Q. Zhang, *J. Mater. Chem. A* **2016**, *4*, 4998.

[15] C. Tang, H. S. Wang, H.-F. Wang, Q. Zhang, G. L. Tian, J. Q. Nie, F. Wei, *Adv. Mater.* **2015**, *27*, 4516.

[16] S. Kattel, G. Wang, *J. Mater. Chem. A* **2013**, *1*, 10790.

[17] a) S. Chen, J. J. Duan, M. Jaroniec, S. Z. Qiao, *Adv. Mater.* **2014**, *26*, 2925; b) X. Y. Lu, W. L. Yim, B. H. R. Suryanto, C. Zhao, *J. Am. Chem. Soc.* **2015**, *137*, 2901.

[18] a) Y. D. Qian, Z. Liu, H. Zhang, P. Wu, C. X. Cai, *ACS Appl. Mater. Interfaces* **2016**, *8*, 32875; b) K. Artyushkova, B. Kiefer, B. Halevi, A. Knop-Gericke, R. Schlogl, P. Atanassov, *Chem. Commun.* **2013**, *49*, 2539.

[19] A. Holewinski, S. Linic, *J. Electrochem. Soc.* **2012**, *159*, H864.

[20] a) G. L. Tian, M. Q. Zhao, D. S. Yu, X. Y. Kong, J. Q. Huang, Q. Zhang, F. Wei, *Small* **2014**, *10*, 2251; b) X. Liu, M. Park, M. G. Kim, S. Gupta, X. J. Wang, G. Wu, J. Cho, *Nano Energy* **2016**, *20*, 315; c) M. Wang, J. Z. Wang, Y. Y. Hou, D. Q. Shi, D. Wexler, S. D. Poynton, R. C. T. Slade, W. M. Zhang, H. K. Liu, J. Chen, *ACS Appl. Mater. Interfaces* **2015**, *7*, 7066; d) Y. Zhan, G. J. Du, S. L. Yang, C. H. Xu, M. H. Lu, Z. L. Liu, J. Y. Lee, *ACS Appl. Mater. Interfaces* **2015**, *7*, 12930; e) D. U. Lee, J. Y. Choi, K. Feng, H. W. Park, Z. W. Chen, *Adv. Energy Mater.* **2014**, *4*, 1301389; f) J. Wang, H. H. Wu, D. F. Gao, S. Miao, G. X. Wang, X. H. Bao, *Nano Energy* **2015**, *13*, 387; g) J. Yin, Y. X. Li, F. Lv, Q. H. Fan, Y. Q. Zhao, Q. L. Zhang, W. Wang, F. Y. Cheng, P. X. Xi, S. J. Guo, *ACS Nano* **2017**, *11*, 2275; h) Y. L. Liu, F. J. Chen, W. Ye, M. Zeng, N. Han, F. P. Zhao, X. X. Wang, Y. G. Li, *Adv. Funct. Mater.* **2017**, *27*, 1606034; i) G. Fu, Z. Cui, Y. Chen, Y. Li, Y. Tang, J. B. Goodenough, *Adv. Energy Mater.* **2017**, *7*, 1601172.

[21] Y. G. Li, M. Gong, Y. Y. Liang, J. Feng, J. E. Kim, H. L. Wang, G. S. Hong, B. Zhang, H. J. Dai, *Nat. Commun.* **2013**, *4*, 1805.

[22] J.-L. Ma, D. Bao, M.-M. Shi, J.-M. Yan, X.-B. Zhang, *Chem.* **2017**, *2*, 525.